Applied Geochemistry 87 (2017) 44–56

Contents lists available at ScienceDirect

Applied Geochemistry

journal homepage: www.elsevier.com/locate/apgeochem

Mineralogical and geochemical characterization of a chromium contamination in an aquifer - A combined analytical and modeling approach

Klaus Philipp Sedlazeck[a,*], Daniel Höllen[a], Peter Müller[b], Robert Mischitz[b], Reto Gieré[c]

[a] Montanuniversitaet Leoben, Chair of Waste Processing Technology and Waste Management, Franz-Josef-Straße 18, 8700 Leoben, Austria
[b] FerroDECONT GmbH, Peter-Tunner-Straße 19, 8700 Leoben, Austria
[c] University of Pennsylvania, Department of Earth and Environmental Science, 240 South 33rd Street, Philadelphia, PA 19104-6316, USA

ARTICLE INFO

Editorial handling by Prof. M. Kersten.

Keywords:
Chromium-contaminated site
Mineralogical characterization
Waste water infiltration
Reduction-induced precipitation
Hydrogeochemical model

ABSTRACT

This study presents a detailed mineralogical and chemical characterization of a chromium contamination in alluvial deposits underlying a leather tannery in Austria. Drill cores revealed that the contamination is represented by a black layer that exhibits sharp boundaries with adjacent brown alluvial sediments. This black layer is located below the groundwater table and begins at the source of the contamination. The black layer thickens with increasing distance from the source and the depth of the upper boundary remains at the same level relative to the surface. Mineralogical and chemical investigations showed that the black layer contains reduced Cr phases, a Cr(III) hydroxide and a Cr(III)-Ca-containing hydrocalcite, which are present as discrete grains, in vein-like pore spaces and/or as a coating around mineral grains. Cr(VI) is nearly only present above the groundwater table. Our 2-D model predicts a longitudinal spread of the black layer of approximately 37 m downgradient from the source and a maximum transversal spread of approximately 10 m. This study shows that, if the source of the contamination is not eliminated, the plume will increase continuously farther downgradient.

1. Introduction

Chromium (Cr), a transition metal, has the atomic number 24. According to Rudnick and Gao (2003), it is the 17th most abundant element in the total Earth's crust (upper, middle and lower crust combined). Its known oxidation states range from −2 to +6 (Cotton and Wilkinson, 1980). In natural environments, however, the only stable oxidation states are +3 and + 6. Even though it is very rare, elemental Cr does occur naturally (Zhu and Liu, 1981). Chemical and physical properties change depending on the oxidation state, which also affects the impact on the environment and human health. Solid phases containing trivalent chromium (Cr(III)) are relatively insoluble and non-toxic to organisms. In small quantities, Cr(III) is an essential dietary element and is required for sugar and fat metabolism in humans and animals (Anderson, 1997). In contrast, hexavalent chromium (Cr(VI)) is extremely toxic and carcinogenic. Most Cr(VI)-bearing solids are also highly soluble. Although the exact consequences of Cr(VI) and Cr(III) uptake in the human body are still debated, the oral and dermal uptake of Cr(VI) is known to cause chronic and acute health effects and, possibly, death (Costa and Klein, 2008; GESTIS, 2006).

Under oxidizing conditions, Cr(VI) is the most thermodynamically stable redox state of Cr. In water, Cr(VI) occurs as chromate, either as H_2CrO_4 under acidic conditions, or in its deprotonated forms $HCrO_4^-$ and CrO_4^{2-} at higher pH. In natural waters, where the pH typically ranges between 3 and 10, the most abundant species are $HCrO_4^-$ and CrO_4^{2-} (Avudainayagam et al., 2003). The chromate ion dimerizes to dichromate ($Cr_2O_7^{2-}$) at high Cr concentrations in the water (Palmer and Puls, 1996). Chromate is a strong oxidizing agent and is readily reduced in the presence of electron donors such as ferrous iron (Fe^{2+}) or sulfite (SO_3^{2-}) and other ions with a lower reduction potential (Wiberg, 1965). If Cr(VI) is reduced, it will most commonly convert into a trivalent cation or neutral $Cr(OH)_3^0$. Upon changes in pH, Cr(III) ions hydrolyze and polymerize. According to Latimer (1952) and Rai et al. (1987), dissolved Cr(III) forms Cr^{3+} ions as well as $Cr(OH)^{2+}$, $Cr(OH)_2^+$, $Cr(OH)_3^0$, $Cr(OH)_4^-$ and $Cr_3(OH)_4^{5+}$ complexes. $Cr(OH)_4^-$ is the only anionic Cr(III) species (Palmer and Wittbrodt, 1991). The predominant species at pH < 4 is Cr^{3+}. At a pH higher than 4, Cr^{3+} hydrolyzes as $Cr(OH)^{2+}$ becomes more stable. The neutral $Cr(OH)_3^0$ species has the widest stability range, from pH 6 to 12 and is therefore the prevailing species in many natural waters. However, predominant speciation can differ from these ideal systems because of the formation of different complexes with other ions in the solution.

* Corresponding author.
E-mail addresses: philipp.sedlazeck@unileoben.ac.at (K.P. Sedlazeck), daniel.hoellen@unileoben.ac.at (D. Höllen), peter.mueller@ferrodecont.at (P. Müller), robert.mischitz@ferrodecont.at (R. Mischitz), giere@sas.upenn.edu (R. Gieré).

http://dx.doi.org/10.1016/j.apgeochem.2017.10.011
Received 6 February 2017; Received in revised form 13 October 2017; Accepted 18 October 2017
Available online 09 November 2017
0883-2927/

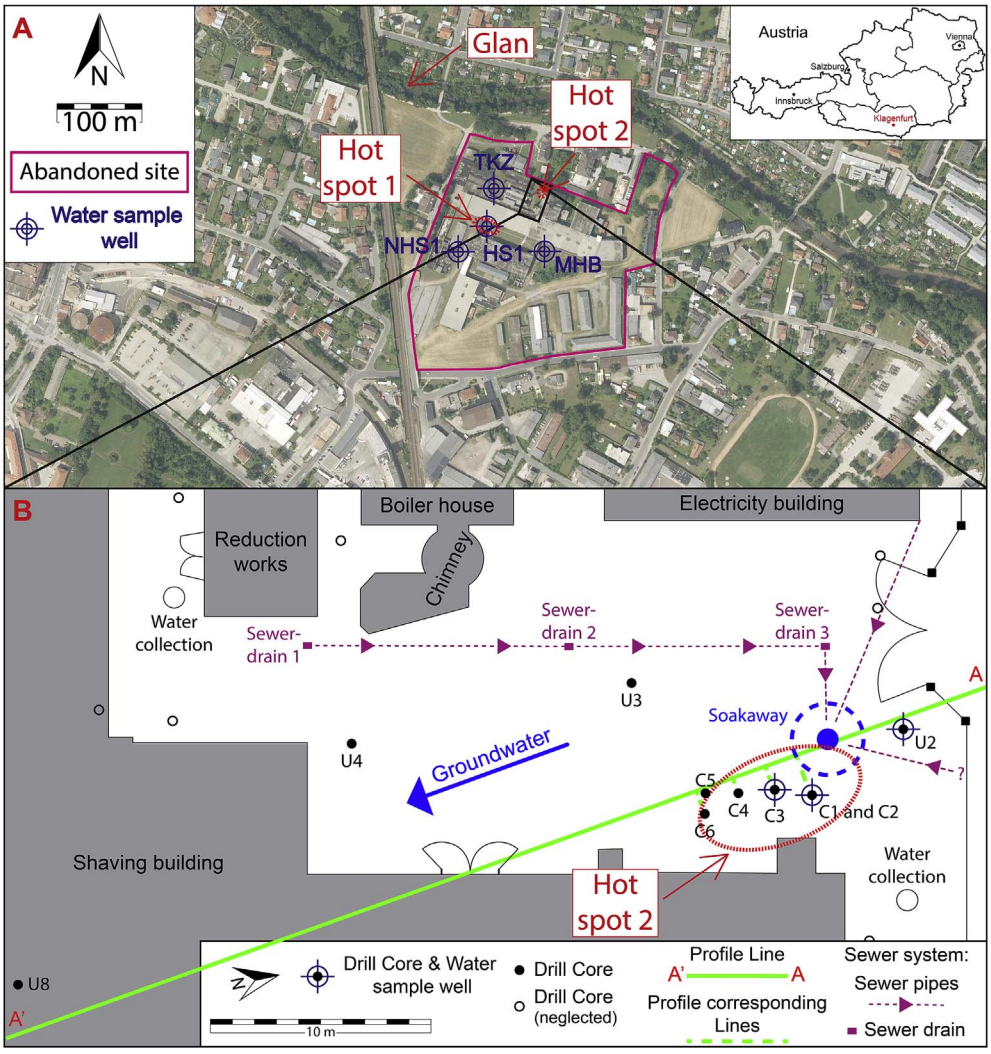

Fig. 1. A: Satellite image from the area northeast of Klagenfurt, marking the abandoned site, groundwater wells where water samples were taken, the study area (the northern part of the contaminated site), the river Glan and the hot spots that were identified (modified from Kagis (2017)). B: Scheme of the northern area of the contaminated site, showing drill core locations (drill cores with black layer identified by C, drill cores without black layer identified by U), groundwater wells, sewer drains and pipes (incl. flow direction), as well as drill sites that are not further considered in this study (modified from Müller et al. (2007)). Groundwater samples presented here were taken from HS1, NHS1, TKZ, MHB, U2, C2 and C3.

Due to its chemical and physical properties, Cr has a wide range of industrial applications, including plating, alloying and tanning. In addition to many further applications, it is used to prevent corrosion by water, as a textile dye and as a pigment (Barceloux and Barceloux, 1999; Petrucci and Harwood, 1993). Spill, leakage, poor storage, improper disposal practices and/or mismanagement in industrial facilities lead to environmental pollution and contaminated sites, which is why a detailed knowledge about the mineralogy and geochemical behavior of Cr in the underground is essential (Calder, 1988; Palmer and Wittbrodt, 1991). The mobility of Cr is controlled by the solubility of the Cr-containing minerals and/or by the adsorption equilibria with specific mineral surfaces or organic materials (Avudainayagam et al., 2003; Chauhan and Sankararamakrishnan, 2011). This mobility has been shown in soils (Bradl, 2004), but it is also relevant in other environmental systems, such as heaps of steel slags (Loncnar et al., 2016).

Thresholds for Cr contamination in groundwater differ from country to country. According to the Austrian risk assessment for contaminated sites (ÖNORM S 2088-1), the threshold for Cr(VI) in groundwater is at 0.01 mg/L, whereas the threshold for further testing in soils is at 50 mg/kg of $Cr_{(tot)}$. Chromium is a common contaminant in the environment and attracts the attention of various researchers, leading to multiple studies on the characterization of Cr contaminations in soils in Europe and elsewhere. Loyaux-Lawniczak et al. (2001), for example, studied the behavior of Cr in soils of a contaminated industrial waste landfill in northern France, and Pawlikowski et al. (2006) described the mineralogy of a Cr contamination, originating from tanning, in river sediments in Poland. The mobility of Cr, derived from ore processing residues has been investigated and modeled by Geelhoed et al. (2001) suggesting that precipitation and co-precipitation are the controlling processes for the mobility of Cr. Gao and Schulze (2010), characterized Cr-contaminated soil samples and reported Cr contaminations in the soil ranging from 13 up 1562 mg/kg. Földi et al. (2013) reported Cr concentrations up to 109 g/kg in samples of waste and soils affected by the production of Cr tanning agents; by using elemental concentrations to distinguish between waste and soil samples. They concluded, however, that the soil samples were generally depleted in Cr. They further found a positive correlation between Ca and Cr. Qafoku et al. (2010) examined the role of reduction in the transport of Cr in acidic waste-contaminated subsurfaces; their column experiments with samples from the vadose zone showed that surface Cr had been reduced by Fe(II) and that Cr-bearing solids are partially associated with Fe(III). Dresel et al. (2008) published a geochemical description of the chromate hot spot in the vadose zone from the same site. Wanner et al. (2012a; b) published a site characterization as well as a transport model, simulating the natural attenuation. Several of these investigations address Cr-contaminated soils and their implications on the environment, but a detailed mineralogical and geochemical characterization of a Cr hot spot situated in the groundwater, combined with a modeling approach that simulates the plume size, has not yet been published.

In this study, we investigate the origin and extent of a Cr contamination at an abandoned leather tannery in Carinthia, Austria. The focus is on a striking black layer that occurs within water-saturated

alluvial deposits beneath an industrial site. We suggest that the contamination originates from an old soakaway, from which residues from the tannery process have infiltrated the alluvial sediments. These residues were discharged into a sewer lane that drains to the soakaway and/or discharged directly into the soakaway. Furthermore, we test our assumption that the Cr was transported by infiltrating water to the groundwater where Cr(VI) was reduced to its trivalent state but continued to spread in the direction of the groundwater flow. We also suggest that the controlling factors for the spreading are precipitation and dissolution reactions. The aim of our mineralogical and geochemical study is to increase our understanding of the ongoing processes in the subsurface of a Cr-contaminated site and to predict the long-term movement of the Cr contamination at the site.

2. Materials and methods

2.1. Site description

2.1.1. Geological and geochemical setting

The samples investigated during our study were taken from the contaminated site *K22 Lederfabrik Neuner*, a leather tannery, northeast of downtown Klagenfurt, located in the Austrian province of Carinthia, approximately 230 km southwest of Vienna. The following general site description is summarized from the official *Contaminated Site Registry* of the Environment Agency Austria (EAA) (Umweltbundesamt, 2013). The abandoned leather tannery occupies an area of 30,000 m^2, half of which is officially classified as contaminated by the EAA (Fig. 1).

Klagenfurt and the contaminated site are located at the northern border of the Klagenfurt Basin, in the area where Neogene and Quaternary sequences were deposited (Nemes et al., 1997). The subsurface of the site consists of alluvial sediments deposited by the river Glan, which is located north of the site (see Fig. 1). Below a thin layer of an anthropogenic filling (1–2 m), the sediments are sandy gravels. These sandy gravels reach a depth of 20 m in the northern area and 10 m in the southern part. In general, the grain size decreases with increasing depth. Below the sandy gravels, there is a layer of fine sand. Lenses with smaller grain sizes, however, are also interlayered within the sandy gravels. These sediment layers form the local aquifer. Underlying the fine sandy sediments are silty clays, which act as an aquitard. The silty clays are encountered at a depth of approximately 35 m in the northern area and approximately 13 m in the southern area.

The groundwater table is ~7 m below the surface, but its depth varies due to natural fluctuations. The overall direction of the groundwater flow is south-southeast (see Fig. 1). This groundwater flow is strongly influenced by infiltration of the river Glan but also by the discontinuous operation (30 L/s in intervals of several minutes per day) of the groundwater pump at the leather tannery. Previous experimental results revealed hydraulic conductivities varying between 2.0×10^{-3} m/s and 1.0×10^{-4} m/s and a hydraulic gradient of 0.5‰ (Umweltbundesamt, 2013).

2.1.2. Industrial use and earlier investigations

The leather tannery has operated since 1922, and achieved its highest production rates in approximately 1961. Today, the manufacturing facilities are no longer used for production purposes, even though the infrastructure is maintained to some extent.

To produce the necessary tannery acid, chromosulfuric acid (H_2CrO_7S) was synthesized on site from potassium dichromate ($K_2Cr_2O_7$) and sulfuric acid (H_2SO_4). Subsequently, this Cr(VI)-containing acid was reduced by the organic reducing agent treacle (molasses) to the Cr(III)-containing tannery acid. Spilling of the chemicals during this process, inadequate waste management, and poor storage practices most likely led to the underground contamination (Umweltbundesamt, 2013).

In 1987, the first groundwater analyses were conducted, revealing the underground contamination. Since then, groundwater samples have been collected periodically from a well (MHB, see Fig. 1A) approximately 90 m downgradient of the investigated hot spot 2 to monitor the Cr contamination. The highest measured Cr concentration (0.54 mg/L) was detected in 1996, with Cr present mostly as Cr(VI). This concentration is much higher than the 0.01 mg/L that is the current Austrian groundwater threshold for Cr(VI). Today, the Cr concentrations in this groundwater well are always approximately 0.1 mg/L, so they are still 10 times above the threshold. The overall Cr(VI) plume in the groundwater spreads ~350 m downgradient of the factory area and shows a maximum transversal extent of ~100 m (Umweltbundesamt, 2013). Exact local background concentrations of Cr in the groundwater are not available, however, the geochemical atlas of Europe (Salminen et al., 2005) provides background concentrations of Cr in stream waters. The median concentration of Cr in stream waters in Europe is at 0.38 µg/L and even lower in the area of the abandoned site (0.210–0.280 µg/L). The groundwater is directly infiltrated by the river Glan, north of the abandoned site (see Fig. 1), consequently, the background concentration in the groundwater can be assumed to be low.

Over the course of many investigations carried out on behalf of the EAA, several holes were drilled and the drill cores were subsequently analyzed for the leaching potential of Cr(VI) (see below) as well as the $Cr_{(tot)}$ concentration. During these investigations, two Cr(VI)-containing hot spots were identified. The hot spot of interest for this study (hot spot 2) is situated in the northern part of the factory area around drill core C1, in the underground between the soakaway and the shaving building (right-hand side of the scheme of Fig. 1B). The dimensions of this hot spot are unknown (Umweltbundesamt, 2013).

2.2. Sample collection

For the research project, as described in Müller et al. (2014), core material was collected from several test holes drilled at the site to install groundwater wells in the spring of 2015. Representative samples were taken from the drill cores by pouring the core material into buckets. Due to the relatively small grain size, it was decided to homogenize the sample by shaking the buckets. Afterwards, the sample was formed into a strip (strip mixing, following ÖNORM EN 15443) and the representative laboratory sample was taken over the entire cross section. To keep the samples as original as possible, they were neither sieved nor ground at this point. The samples were dried (105 °C), and part of the sample was finely ground for bulk chemical analysis. Sample C3 (see Fig. 1) from a depth between 9 and 10 m was chosen for detailed chemical and mineralogical analyses.

Groundwater samples were taken according to the contaminated groundwater sampling norm (ÖNORM S 2092) and preserved as described in ISO 5667-3. Sample collection started after a minimum of 10 min of pumping, and a constant electric conductivity and pH were reached. On-site parameters (electric conductivity, pH, Eh and the O_2 concentration) were measured immediately, according to DIN EN 27888, ISO 10523, DIN 38404-6 and DIN EN 25813. The redox potential was determined by using a Ag/AgCl 3 M KCl electrode, and measured data were subsequently corrected to the standard hydrogen electrode. For the cation analytics, the sample was stored in borosilicate glass, and HNO_3 was added to reach a pH between 1 and 2. Samples for anion analyses were stored in a glass vessel. Samples TKZ, NHS1, HS1 and MHB were taken during our groundwater investigations in the beginning of April 2014, and U2, C2 and C3 were collected in the middle of May 2015. All samples were cooled during transportation to the laboratory and analyzed as soon as possible.

During our investigations, the sewer system of the area west of hot spot 2 was mapped in detail (see Fig. 1B). In addition, we collected two samples of black sludge, which were recovered from sewer drains 1 and 2 (see Fig. 1B) and subsequently analyzed for their $Cr_{(tot)}$ content and for leachable Cr(VI).

2.3. Mineralogical and chemical analyses

Powder X-ray diffraction (XRD) analysis of the finely ground sample C3 (9–10 m) was performed to obtain mineralogical information about the contaminated alluvial sediment by using a PANalytical X'Pert Pro, operated with Co-Kα radiation at 40 mA, 45 kV and sample rotation. XRD data were collected in a 2θ angle range between 4° and 110° and an increment of 0.02°. Rietveld refinement was applied after Allmann (2003).

To better understand the distribution and the mineralogy of Cr in the underground, electron microprobe (EMP) analyses were performed. These analyses were carried out with the original, dried and non-ground sample C3, embedded in epoxy resin. The embedded sample was subsequently polished, sputtered with carbon and directly mounted onto a sample holder. The Superprobe JEOL JXA 8200, installed at the Eugen F. Stumpfl Laboratory at the Montanuniversitaet Leoben, Austria, was used. During quantitative analyses as well as for element mapping, the EMP was operated in wavelength-dispersive spectrometer (WDS) mode, with an accelerating voltage of 15 kV and a beam current of 10 nA. All elements were analyzed using their Kα lines, and they were calibrated on natural chromite (Cr, Al), rhodonite (Mn), wollastonite (Si, Ca), magnetite (Fe, O), apatite (P), and sphalerite (S). The following diffracting crystals were used: LDE1 for O; TAP for Al; PETJ for Si, Ca, S and P; and LIFH for Cr, Mn and Fe. Counting times on peak and background were 20 and 10 s, respectively.

Bulk-rock analyses of the drill core material, including total Cr concentration, were conducted by using an inductively coupled plasma mass spectrometry (ICP-MS) system from Agilent (Type 7500) at the Chair of Waste Processing Technology and Waste Management, Montanuniversitaet Leoben. Prior to analysis, the material was digested in HF and aqua regia using a microwave digestion system according to ÖNORM EN 13656. The elemental concentrations reported here have been determined during this study as described in the ÖNORM EN ISO 17294-2, augmented by additional data collected during previous work from Müller et al. (2007) and UTC (2012).

The leachability of Cr(VI) from the solids was investigated according to the procedures described by the DIN 38414-4, i.e., by shaking the original sample material in deionized water for 24 h with a liquid-to-solid weight ratio of 10:1. The Cr(VI) concentration in the liquid was then determined photometrically as explained in DIN 38405-24.

2.3.1. Water chemistry analytical methods

Cations in the water samples were measured by ICP-MS (see above) and anion concentration analyses were performed with an ion chromatography system DIONEX – IC (ICS 2000) after ÖNORM EN ISO 10304-1. The HCO^{3-} content was determined by titration with 0.1 moL/L HCl, according to DIN EN ISO 9963-1.

2.4. Description of the hydrogeochemical model

A two-dimensional (2-D) hydrogeological and hydrogeochemical reactive transport model was developed for the saturated zone to deliver supplementary information and to interpolate between drill holes. This modeling was conducted by using the software X2t from Geochemist's Workbench (version 11 professional) and the provided database thermo_minteq.tdat, which is based on Visual MINTEQ release 2.40. The main idea of the model is that the groundwater, moving through the domain being investigated, is infiltrated by contaminated water from the leather tannery. The chosen time interval was 100 y. Even though it is a 2-D model, a volume is required to model groundwater flow. Therefore, the domain dimension was chosen as 50 × 40 × 1 m. A groundwater discharge rate of 0.5 m/d and an aquifer porosity of ~20% have been determined experimentally (Umweltbundesamt, 2013). For the model, a porosity of 19 ± 1% was chosen to simulate the underground heterogeneity. To simulate the contamination source (soakaway, see chapter "Discussion"), we defined five injection wells, four of which were arranged in a circular shape around one center well.

To reduce calculation times, the predefined waters for the simulation were kept as simple as possible. Hence, they only contained Na and Cl for charge balance. The initial pH was set to 7.7 in the groundwater, as measured at the beginning of the project. For the contaminated water, the pH was assumed to be 6.0, based on the presence of chromosulfuric acid. Standard-state temperature was chosen. Based on data collected as part of this study and on previous groundwater analyses from the EAA, the CrO_4^{2-} concentration was set to the following values: 1.16×10^{-13} mg/L for the uncontaminated groundwater (Cr(VI) concentrations were below the detection limit but an initial concentration had to be defined for the simulation) and 17 mg/L for the contaminated water that infiltrates the system via the injection wells that simulate the source (soakaway). To establish reducing conditions, the fugacity of O_2 was set to $10^{-25.0}$ for both waters, which forces reduction of Cr and consequently precipitation of Cr solid phases.

Our mineralogical investigations revealed that a Cr-bearing phase precipitated, leading to the formation of the black layer (see "Results" section below). For this reason, the anticipated solid phase to precipitate in our model is $Cr(OH)_{3(am)}$. After the reduction of introduced Cr(VI), hydrolysis of Cr(III) generates Cr(III)-hydroxide complexes and consumes OH^- ions, which causes a decrease in pH. Thus, a pH buffer was implemented by adding 0.1 moL/kg of amorphous Fe(II) hydroxide ($Fe(OH)_{2(am)}$) as a reactant mineral phase into each model cell. Precipitation of undesired phases was prohibited by suppressing: a) the Cr-bearing phases Cr_{metal}, $Cr(OH)_2$, $Cr_2O_{3(c)}$, $CrCl_2$, $CrCl_3$, CrO_3, and $FeCr_2O_4$, and b) the Fe-bearing phases $Fe(OH)_{2.7}Cl_{0.3}$, ferrihydrite, $ferrihydrite_{(aged)}$, goethite, hematite, lepidocrocite, maghemite, and magnetite.

The diffusion coefficient was set to default, i.e., 1.0×10^{-09} cm^2/s. This value is slightly higher than the 0.59×10^{-09} cm^2/s proposed by Yuan-Hui and Gregory (1974), but test calculations showed that slight changes of the diffusion coefficient did not affect the output of our model significantly. The combination of a low flow rate and the above diffusion coefficient leads to a relatively low (< 1) Péclet number (*Pe*). According to Bijeljic and Blunt (2007), a low *Pe* means that transversal dispersion is equal to the longitudinal dispersion. The dispersivity in our model was determined through trial and error. Measured $Cr_{(tot)}$ and Cr(VI) concentrations in the sedimentary materials of drill cores U3, U4 and U8 (see Fig. 1) were compared to the calculated concentrations to evaluate the modeling results. Remaining inputs were set to default values of Geochemist's Workbench, i.e., thermal conductivity = 0.004 caL/cm/s/C; heat capacity: cpw (fluid): 1 caL/g/C and cpw (minerals): 0.2 caL/g/C; internal heat source = 0.0 $caL/cm^3/s$; permeability: A (porosity) = 15, B (intercept) = −5.0 darcy, Kx/Ky (anisotropy) = 1.0.

2.5. Eh-pH diagram calculation

The predominant species in the system were calculated by using the software Act2 from Geochemist's Workbench (Student version 11.0.5). The applied database was the same as for the groundwater model (thermo_minteq.tdat), but for the computation of Eh-pH diagrams, the database had to be slightly modified. The original database does not contain the species $H_2(g)$, which is required to calculate the stability field of water. Data for this species were copied and implemented from the LLNL-based thermos.tdat database (version from October 2013).

Input concentrations for the calculations were derived based on the measured groundwater concentrations (see section "3.1 Chemical composition and color" below); the activity was assumed to equal the measured concentrations (activity coefficient equals unity). Since Cr and Fe must have been present in relatively high quantities during precipitation (see section "3.2 Mineralogical composition"), the activities were set to 3.80×10^{-05} (Cr) and 3.54×10^{-05} (Fe; both 2 mg/L)

for these calculations. The diagram was calculated at 25 °C. Suppressed phases were: Cr(VI)-Ettringite, Cr(VI)-Jarosite, Cr_2O_3 (c), $Fe(OH)_2$ (am), $Fe(OH)_2$ (c), $Fe(OH)_{2.7}Cl_{0.3}$, $Fe_3(OH)_8$, $FeCr_2O_4$, Ferrihydrite, Ferrihydrite (aged), Goethite, Greenalite, Hematite, Hercynite, K-Jarosite Lepidocrocite, Maghemite, Magnesioferrite, Magnetite, $MgCr_2O_4$, and Siderite.

3. Results

3.1. Chemical composition and color

Macroscopic observation of the drill cores (labeled with C, Fig. 1B) downgradient from hot spot 2 revealed a sudden change in color of the alluvial deposits at a depth of approximately 9 m. Drill core C6, for example, seen in Fig. S1A (Supporting Material), showed the abrupt transformation from the typical brownish color of the upper sedimentary layers to a distinctly black color at a greater depth at 9 m below the surface. This dark layer, referred to as the black layer below, occurs underneath the groundwater table, which is located ~7 m below the surface.

Some of the core material exhibits a change in grain size from sandy gravel to fine sand at the same depth where the distinct color change occurs; in these drill cores, the sediment below the black layer consists of sandy gravel again. However, the black layer is not associated with a change in grain size in all of the available drill cores. Drying of the originally dark black, wet material led to a distinct color change to a greenish gray color. The original mineral grains seem to be coated with greenish precipitates, which appear black when wet. For the original brown uncontaminated sample, drying did not lead to a drastic color change (see Figs. S1B and C).

Fig. 2 shows profiles for each of the drill cores from the area adjacent to hot spot 2 (see Fig. 1). The drill-core diagrams are arranged from north to south, along the groundwater flow direction. The upper boundary of the black layer descends to ~9 m, and the thickness of this black layer increases simultaneously to a maximum of 4.2 m.

Drill core C2 was collected to confirm the reported hot spot 2 (C1) from previous studies. Alluvium from core C2 shows the color change from brown to black and black to brown at depths of 9 m and approximately 9.7 m, respectively. The observed maximum thickness of 4.2 m was found in C6 between a depth of 9 m and 13.2 m. Drill cores C3, C4, and C5 confirm the thickening with increasing distance from the soakaway, with local small-scale variations. Drill cores C5 and C6 were the farthest downgradient, and therefore no additional direct information about the depth and extent of the black layer is available. The first meter of C1 as well as core material from a depth between 3.8 m and 6.6 m exhibit a gray color (see Fig. 2). Gray-colored drill core material was also discovered from drill cores C3 (8–9 m) and C4 (8.7–9.7 m).

In addition to displaying sediment color, Fig. 2 shows the measured $Cr_{(tot)}$ concentrations in the drill cores as well as analytical data from the shaking experiments. Altogether, the measured $Cr_{(tot)}$ concentrations in the black layer range from 270 mg/kg to 9600 mg/kg; these extreme values were both found in drill core C4 at depths of 10.7 m–11.5 m and 9.7 m–10.7 m, respectively.

No color change was observed in drill cores U2, U3, U4 and U8. However, $Cr_{(tot)}$ concentrations of up to 2690 mg/kg were recorded in drill core U3. This high concentration was found below the groundwater table at a depth of 7.8–8.7 m, i.e., slightly above the depth where the black layer was present in the wells, marked with a “C”. This maximum concentration is much higher than the lowest $Cr_{(tot)}$ concentrations within the black layer (C4, see Fig. 2). Similarly, high $Cr_{(tot)}$ concentrations above the black layer were found in other drill cores, e.g., in C1 (2800 mg/kg at 3.8 m–5.8 m and 2400 mg/kg at 6.6 m–8.6 m).

Leached Cr(VI) from the drill core samples is also presented in Fig. 2. Extractable Cr(VI), with concentrations ranging from 2.8 to 8.8 mg/kg, was present in brown and gray alluvium from sites C1 and C2, nearest the soakaway. No extractable Cr(VI) was present in black-stained alluvium except in C1, at a depth between 8.6 m and 10 m. However, this Cr(VI) concentration was by far the lowest measured concentration (0.08 mg/kg). Leachates from C6 and U3 were the only leachates that contained Cr(VI) outside the immediate vicinity of the soakaway, but the Cr(VI) concentrations in leachates from these two drill cores are considerably lower than the Cr(VI) concentrations from the brown sediments in C1 and C2.

The macroscopic observations were used to construct the section A–A’ (Fig. 3), which is oriented parallel to the groundwater flow (Fig. 1). Projection of drill holes on the section are shown in Fig. 1B. The black layer present within the drill cores is shown in black in this profile, whereas the gray-colored area represents the presumed extension of the contamination as inferred from modeling results (see below). Visual observation shows that the black layer pinches out near the soakaway and was not present in cores drilled directly upgradient from the soakaway.

Our on-site investigations revealed that a total of three sewer drains connect to the main sewer line, which itself drains into the soakaway (Figs. 1B and 3). In close vicinity to the soakaway, the tannery acid was produced in the reduction works building. The main sewer pipe starts at sewer drain 1 in front of this building (see Fig. 1B). In addition to the water from the main sewer line, a large portion of the collected surface waters is also channeled into this soakaway via other lines (magenta dashed lines with arrows in Fig. 1B). The soakaway reaches a depth of approximately 4 m (Fig. 3). In this soakaway, bare sediments are exposed, so the collected waters discharge directly into the alluvial deposits, which form the aquifer. The black sludges that were recovered from sewer drains 1 and 2 (see chapter 2.2) exhibit very high $Cr_{(tot)}$ concentrations, i.e., 54,400 mg/kg (sewer drain 1) and 66,100 mg/kg (sewer drain 2).

The composition of seven groundwater samples, taken from seven groundwater wells distributed on the factory area, is provided in Table 1, which also lists the mean ion concentrations used as input for the 2-D modeling (chapter 3.4).

Measurements of the field parameters revealed a neutral to slightly alkaline pH (7.0–8.0) and an electric conductivity varying between 500 and 600 µS/cm. The prevailing Eh was determined to be approximately 300 mV with local variation. Samples taken from groundwater wells installed where the black layer is present (i.e., C2 and C3) have the lowest Eh values. The concentrations of dissolved O_2 ranged from 0.3 to 8 mg/L in all samples.

The data indicate that bicarbonate is the major anion, whereas the major cations in solution are Ca^{2+}, Na^+ and Mg^{2+}. Iron was present mostly in concentrations below or approximately at the quantitation limit of 0.01 mg/L; however, the sample from C3 exhibited an Fe concentration of 1.68 mg/L, which was by far the highest measured concentration. Cr concentrations ranged from < 0.001 to 0.44 mg/L. If Cr was present in groundwater samples taken from outside the area of the black layer (U2, HS1 and MHB), between 63% and 98% was present as Cr(VI).

3.2. Mineralogical composition

Quantitative XRD analysis yielded a composition of 66 wt% quartz, 16 wt% albite, 10 wt% muscovite, and 7 wt% chlorite for a sediment sample from drill core C3 (9–10 m), where the black layer was present (Sedlazeck et al., 2015). The corresponding XRD pattern is displayed in the appendix (Fig. S2, Supporting Material).

To obtain additional information regarding the mineralogical composition of the black layer, a sample from drill core C3 was further studied by EMP and ICP-MS analysis. This sample, collected from a depth of 9 m–10 m, contains nearly 3 g/kg of $Cr_{(tot)}$ (see Fig. 2). Fig. 4 shows element distribution maps from an area (point of interest 1, POI 1) within this sample. The element maps document that a Cr-bearing phase precipitated in a vein-like pore space, which is bordered by

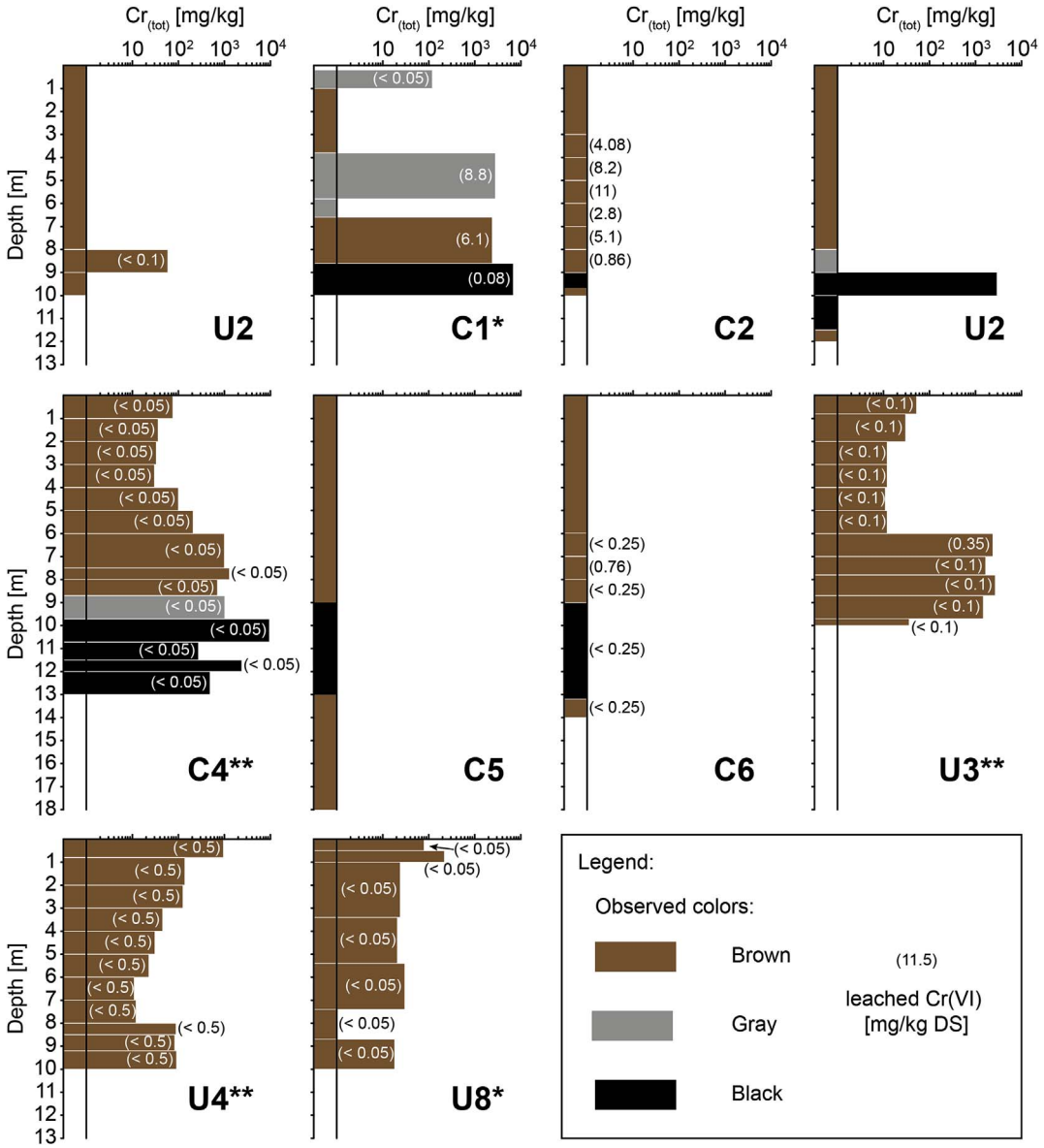

Fig. 2. Observed color (between the two vertical lines), $Cr_{(tot)}$ concentrations, and concentrations of leached Cr(VI) for the available drill cores adjacent to hot spot 2, arranged from north to south along the direction of groundwater flow. For drill core locations, see Fig. 1. * data from UTC (2012); ** data from Müller et al. (2007). (For interpretation of the references to colour in this figure legend, the reader is referred to the web version of this article.)

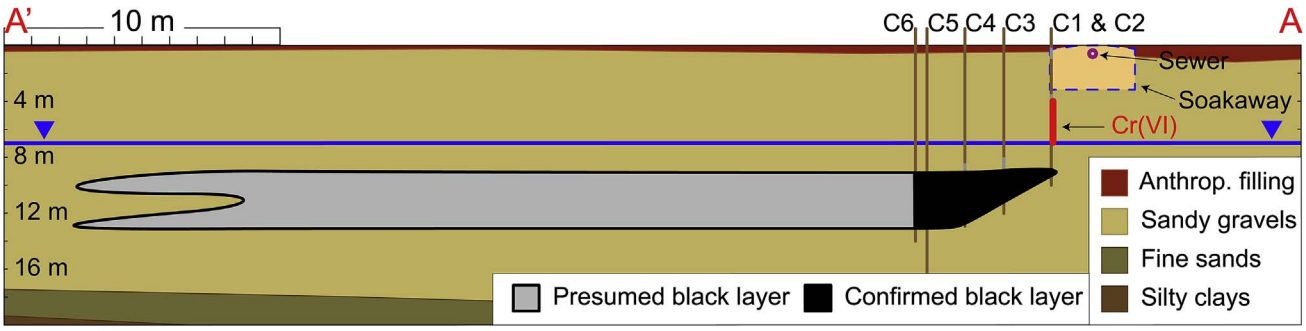

Fig. 3. Section A-A′ parallel to the groundwater flow (from right to left) through the contaminated area (see Fig. 1). Vertical scale compressed twice. Drill cores C1 through C6, exhibiting the black layer, are shown, as is the groundwater level at a depth of ~7 m.

quartz and alkali feldspar. Areas with a high Cr content have low Fe concentrations and vice versa (compare Fig. 4C and D). The maps further reveal that Cr is associated with Ca and O (Fig. 4B, C and E), whereas Fe is associated with S (Fig. 4D and F). Quantitative analyses (Table 2) could not yield the exact stoichiometry of the solid phases, but the element distribution maps indicate that a Fe sulfide, probably pyrite, as well as a Cr oxide/hydroxide, probably $Cr(OH)_3$, precipitated in this pore space. During the attempt to acquire the quantitative EMP

Table 1
Measured pH, Eh, electric conductivity and O_2 concentration as well as ion concentrations from seven groundwater samples, taken from groundwater wells located in the factory area. Mean concentrations are also provided in mg/L and mmol/L. No mean concentration provided for $Cr_{(tot)}$ and $Fe_{(tot)}$ because concentrations ranged to values below the quantitation limit (Cr: < 0.001 mg/L and Fe: < 0.01 mg/L). Sampling conducted beginning of April 2014 (TKZ, NHS1, HS1 and MHB) and middle of May 2015 (U2, C2 and C3).

		U2	C2	C3	TKZ	NHS1	HS1	MHB			
pH	–	7.2	7.3	7.6	7.9	7.2	7.1	7.9			
Eh	mV	366	270	222	297	335	494	373			
el. cond.	µS/cm	534	562	557	533	528	583	520	**Mean concentration**		
$O_{2(aq)}$	mg/L	3.3	2.7	0.3	0.56	7.47	6.6	8	**(n = 7) mg/L**	**σ_{n-1} mg/L**	**(n = 7) mmol/L**
Ca^{2+}	mg/L	92	77.5	62.5	61.5	61.7	95	89.4	77	15.2	1.92
Mg^{2+}	mg/L	14.4	11.7	13.4	12.5	15.3	17.5	12.1	13.8	2.1	0.569
Na^{+}	mg/L	18.8	17.9	16.1	16.3	13.4	12.9	15.7	15.8	2.2	0.687
K^{+}	mg/L	4.05	3.99	4	3.93	4.2	3.6	3.81	3.95	0.2	0.101
$Fe_{(tot)}$	mg/L	0.21	1.35	1.68	0.19	< 0.01	< 0.01	0.076	< 0.01–1.68	–	–
Al^{3+}	mg/L	1	0.94	1.2	0.91	0.94	0.99	0.98	0.99	0.1	0.037
$Cr_{(tot)}$	mg/L	0.16	0.29	0.23	< 0.001	< 0.001	0.44	0.079	< 0.001–0.44	–	–
Cr(VI)	mg/L	0.10	0.12	< 0.05	< 0.05	< 0.05	0.43	0.06	< 0.05–0.43	–	–
$Mn_{(tot)}$	mg/L	0.98	1.05	0.95	0.97	1.2	0.9	0.92	1	0.1	0.018
SiO_2	mg/L	0.06	0.05	0.06	0.06	0.05	0.02	0.09	0.06	0.02	0.001
HCO_3^{-}	mg/L	289	305	209	207	239	307	201	251	48	4.11
SO_4^{2-}	mg/L	31.4	29.7	32.2	54.5	34.4	50.2	30.5	37.6	10.3	0.391
Cl^{-}	mg/L	16.8	18.1	17.4	16.9	20	16.7	19	17.8	1.3	0.501
F^{-}	mg/L	0.11	0.15	0.11	0.08	0.14	0.14	0.14	0.12	0.03	0.006
NO_3^{-}	mg/L	24	19	19.5	31.6	28.8	9.5	26.7	22.7	7.5	0.366

data from this material, the electron beam imparted significant damage to the analysis spots, resulting in rather low-quality quantitative data. Exact measuring spots are shown in Fig. 4A.

The positive correlation between Cr and Ca in the element distribution maps (Fig. 4B and C) suggests that the inferred $Cr(OH)_3$ might actually be a Ca-Cr-phase. A search in the ChemSpider database (Royal Society of Chemistry, 2015) revealed that there are several Ca-Cr-containing chemical compounds. Most of these compounds contain hexavalent chromium, but our leaching results suggest that in the black layer, Cr is present in its trivalent rather than hexavalent form (Fig. 2). No matching Ca-Cr(III)-bearing hydroxide was found in the ChemSpider database, but an unnamed hydrocalcite containing Cr(III) and Ca has been described in the literature (Grguric et al., 2006). This mineral has the idealized formula $CaCr_2^{3+}(CO_3)_2(OH)_4{\cdot}H_2O$ and is a Ca-analog of petterdite, a Pb-Cr(III)-containing member of the dresserite mineral group.

Element distribution maps of Ca, Cr, Fe, O and S of another area in sample C3 (POI 2) are presented in Fig. 5. The grain exhibits Cr-Ca-O and Fe-S distribution features that are very similar to those observed in Fig. 4. However, the Fe-S phase and the Cr-oxide/hydroxide phase are not as clearly separated, but rather occur in close proximity, even in contact with each other. Calcium contents are also in the same range as those found in POI 1 (Table 2, for analysis locations, see Fig. 5A). Also notable are the thin (up to 1 µm) Cr-containing coatings on quartz and alkali feldspar grains (Fig. 5C). The coatings also contain some Ca but contain neither Fe nor S (Fig. 5B, D and F).

3.3. Phase relationships

A simplified Eh-pH phase diagram of the groundwater system showing predominant species of Cr and Fe is provided in Fig. 6. This figure is a stacked and combined version of the two individually calculated Eh-pH diagrams provided in Fig. S3 (Supporting Material). The diagrams were calculated at 25 °C and are based on the mean groundwater analysis, provided in Table 1.

Phases of interest are chromium hydroxide (i.e., $Cr(OH)_{3(am)}$, presented in green) and iron sulfide (i.e., pyrite (FeS_2), shown in yellow), which were inferred to be present from our EMP investigations. Several phases were excluded from the calculations because they were not detected during the mineralogical analysis (section 3.2). Suppressed phases were: Cr(VI)-Ettringite, Cr(VI)-Jarosite, Cr_2O_3 (c), $Fe(OH)_2$ (am), $Fe(OH)_2$ (c), $Fe(OH)_{2.7}Cl_{0.3}$, $Fe_3(OH)_8$, $FeCr_2O_4$, Ferrihydrite, Ferrihydrite (aged), Goethite, Greenalite, Hematite, Hercynite, K-Jarosite Lepidocrocite, Maghemite, Magnesioferrite, Magnetite, $MgCr_2O_4$, and Siderite. Unfortunately, no thermodynamic data are available for the inferred hydrocalcite phase.

Fig. 6 documents that $Cr(OH)_{3(am)}$ (green) and pyrite (yellow) can occur together in reducing, slightly acidic to alkaline environments. Pyrite is also stable in more acidic environments, whereas $Cr(OH)_{3(am)}$ can exist in conditions that are more oxidizing than those outlined by the stability field of pyrite. The star represents currently prevailing Eh-pH conditions of the groundwater (see chapter 3.1) in the studied area and shows that $Cr(OH)_{3(am)}$ is the thermodynamically stable solid phase and is expected to precipitate in the system.

The star also indicates that the prevailing dominant aquatic species consist of ferrous Fe and trivalent Cr. As described in the previous section, pyrite and $Cr(OH)_{3(am)}$ [+Ca-Cr-hydrocalcite] precipitated spatially separated from each other at POI 1, whereas at POI 2 they occur together in one grain, consistent with the stability fields of the Eh-pH diagram in Fig. 6. Combining the EMP analyses results with the Eh-pH diagram yields two different evolution scenarios of the precipitated solid phases.

3.4. 2-D modeling

Because direct information regarding the extent of the Cr contamination is limited to a few drill cores, a 2-D model was calculated to assess the distribution of the precipitated trivalent Cr hydroxide ($Cr(OH)_{3(am)}$), which is inferred to be the major Cr-bearing solid phase in the black layer within the alluvium downgradient from the soakaway. The result of this model is shown in Fig. 7.

By changing parameters, which were not determined on site (e.g., the Cr concentration of the water that infiltrates the system through the soakaway, or the infiltration rate of this water), the plume was simulated at a depth of 9–10 m by trial and error. The accuracy of the model was verified by comparing calculated Cr concentrations to the chemical analyses of the core material (Fig. 2). Similarly, we also used the presence or absence of the black layer in these drill cores as constraints for the lateral extent of the contamination.

The model results (Fig. 7) suggest that the black layer spreads with the direction of groundwater flow in a typical plume shape, with higher Cr concentrations in the alluvium near the contamination source (soakaway) rather than farther downgradient. According to the model, the black layer has a longitudinal spread of approximately 37 m

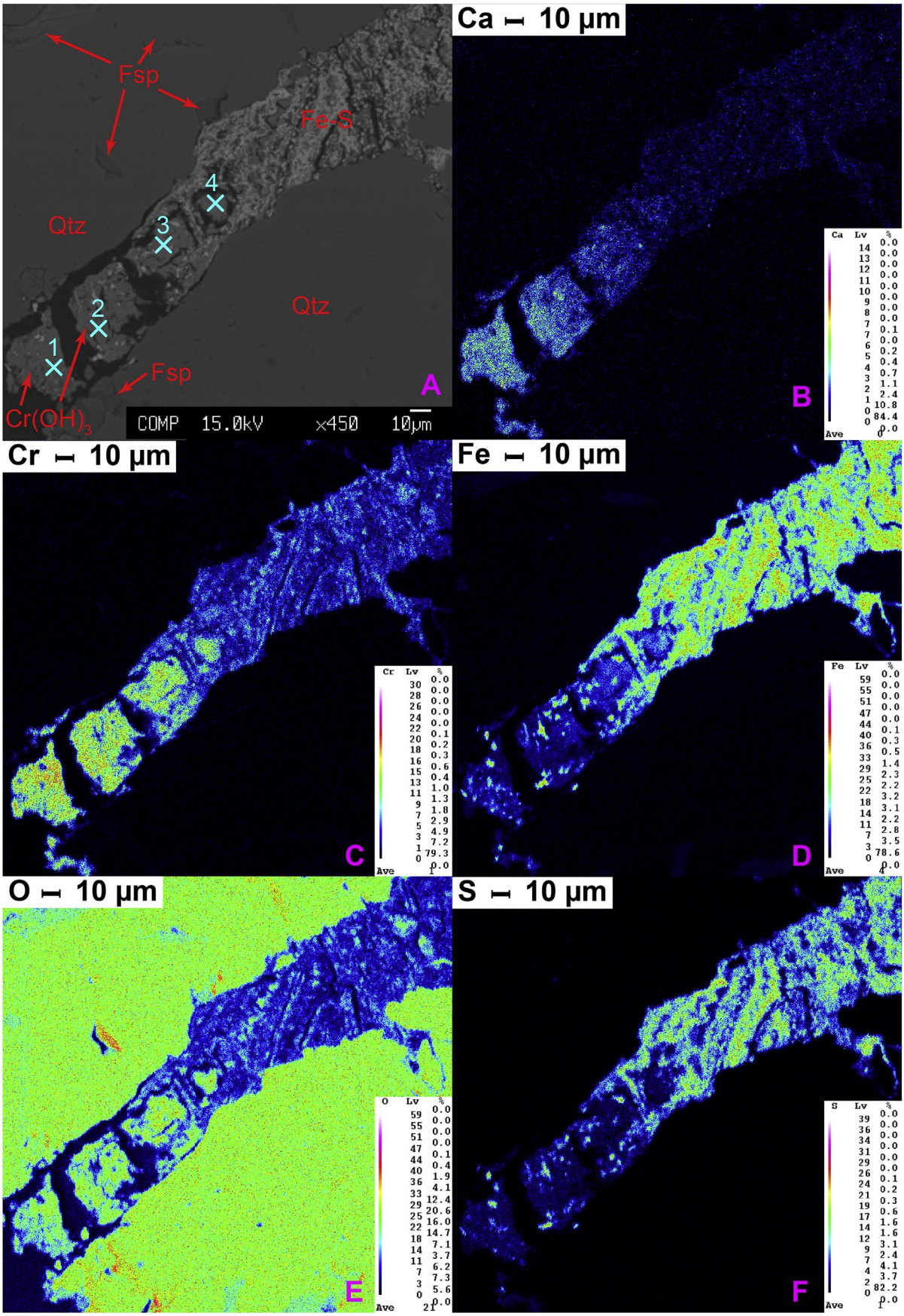

Fig. 4. Sample material from the black layer in the contaminated drill core C3 (POI 1): (A) Back-scattered electron (BSE) image, with marks indicating where the WDS analyses given in Table 2 were made. Element maps showing the distribution of Ca (B), Cr (C), Fe (D), O (E), and S (F). The BSE image and the element distribution maps display precipitates of Fe-S and Cr phases in a vein-like pore space, which is bordered by quartz (Qtz) and alkali feldspar (Fsp).

Table 2
Quantitative EMP analysis data from sample C3 POI 1 (Fig. 4) and POI 2 (Fig. 5).

Nr.	O mass %	Al mass %	S mass %	P mass %	Cr mass %	Si mass %	Ca mass %	Fe mass %	Mn mass %	Total mass %
POI 1										
1	36.49	1.77	4.75	0.555	27.33	0.523	4.06	4.48	0.088	80.04
2	39.18	2.73	5.45	0.541	28.08	0.698	3.96	5.32	0.132	86.08
3	41.06	3.78	5.42	0.505	25.03	1.06	1.69	10.98	0.115	89.64
4	35.15	3.66	5.02	0.559	21.37	1.20	1.01	18.38	0.097	86.46
POI 2										
5	43.12	1.38	5.80	0.582	32.06	0.627	3.33	1.33	–	88.22
6	39.67	1.03	5.17	0.627	32.82	0.744	2.81	2.28	–	85.15
7	37.72	1.05	4.90	0.611	31.14	2.32	2.22	5.83	–	85.79
8	–	1.88	15.37	1.405	47.54	0.808	4.62	1.61	–	73.22
9	41.83	1.18	5.35	0.616	33.58	0.446	3.01	1.74	0.115	87.86

downgradient from the soakaway and a maximum transversal spread of approximately 10 m.

Due to the relatively low flow velocity of the groundwater and resulting high diffusion, the area 2–3 m upgradient of the soakaway is also affected by the contamination. Overall, the model is consistent with the Cr distribution as measured in the available drill cores at a depth of 9–10 m (Fig. 2).

4. Discussion

After encountering the black layer during the drilling campaign, questions arose about the nature and extent of this layer. It was not clear whether the black layer is anthropogenic and related to the contamination at the site, and drill core locations provide only very small-scale and scattered information about the lateral extent of the black layer.

The water table near the abandoned site is at ~7 m below the surface (see Fig. 3), which means that the black layer occurs at least 1.7 m below the groundwater table. The black layer pinches out near the soakaway, indicating that this point is the source of the contamination. The main sewer pipe starts in front of the reduction works building (sewer drain 1 in Fig. 1B), which gave rise to the assumption that both Cr(VI)- and Cr(III)-contaminated materials (liquids, solids and sludge) were discharged to the sewer system. The released contaminated substances infiltrated via the soakaway into the subsurface, subsequently reaching the groundwater. This assumption is also supported by the black, Cr-rich sludge that was found during the mapping in sewer drains 1 and 2.

Drying of the originally dark black, wet core material causes the color to change to greenish gray (Fig. S1B), which points to the possible presence of trivalent Cr. This assumption is also supported by the analytical data from the shaking experiments because Cr(VI) was leached only from the brown and gray sedimentary material and not from the black samples (except for C1; see Fig. 2). Due to high Cr(VI) concentrations in leachates from drill cores C1 and C2, we conclude that the majority of leachable Cr(VI) is present in the brown sedimentary material above the groundwater, near the soakaway. The source of the Cr(VI) contamination in the vadose zone, as well as in the groundwater fluctuation zone in C6 and U3, is not clearly understood, but it might originate from diffuse dissemination of Cr(VI). The geochemical conditions in this area were apparently not reducing enough to transform the Cr(VI) to Cr(III).

Investigated water samples revealed that the pH ranged between 7.1 and 7.9, and Eh ranged between 220 and 490 mV. According to the calculated Eh-pH diagram, the predominant Cr species under these conditions is Cr(III). However, in some groundwater samples, Cr was present in its hexavalent state, even though it is thermodynamically not favored. A reduction reaction is prevented kinetically. The Cr(VI) present in the groundwater must have infiltrated from overlying sediments, because the Cr(VI) source is in the vadose- and/or groundwater-fluctuation zone, where Cr(VI) is stable.

Chromium can be present in the samples either as precipitated discrete Cr-bearing phases or sorbed onto mineral surfaces (e.g., amorphous Fe hydroxide). We interpret the EMP analyses as evidence for precipitation of Cr-bearing phases and, consequently, we conclude that sorption is not the controlling mechanism for the mobility of Cr. Unfortunately, no Cr-bearing phase could be detected by XRD. This result is due either to such phases being absent or are present in concentrations below the XRD detection limit (~2 wt%) or to the presence of amorphous hydroxide phases. However, the lack of a hump-shaped feature in the lower 2θ range of the XRD pattern suggests that non-crystalline phases are not present or present at only very low concentrations. During the mineralogical analysis (EMP and Raman spectroscopy), we observed severe damage to the sample caused by both the electron beam and the laser beam, and thus, we interpret that Cr is present within phases such as $Cr(OH)_3$ and/or Ca-Cr-hydrocalcite with poorly crystalline and/or amorphous structure.

The Ca-Cr-hydrocalcite phase precipitated along with Cr hydroxide, and this mixture was analyzed by EMP. The interpretation of the Ca-Cr-containing phase being Ca-Cr-hydrocalcite is also supported by the groundwater analysis (Table 1), which documents that bicarbonate and Ca^{2+} are the major ions in solution. However, a precipitate consisting of pure Ca-Cr-hydrocalcite can be excluded because the Ca concentrations detected in the solid are too low to fulfill the idealized stoichiometry of the mineral formula, $CaCr_2^{3+}(CO_3)_2(OH)_4{\cdot}H_2O$ (Grguric et al., 2006). Minerals such as the spinel-type phase $CaCr_2^{3+}O_4$, which was identified in steel slags by Höllen et al. (2016), would not have been destroyed as easily by the laser or electron beams and can therefore be excluded. Other Cr phases such as Cr(III)-ettringite (bentorite), $Ca_6(Cr^{3+},Al)_2(SO_4)_3(OH)_{12}{\cdot}26H_2O$ and Cr(VI)-ettringite, $Ca_6Al_2((Cr^{6+},S)O_4)_3(OH)_{12}{\cdot}26H_2O$, as reported by Sokol et al. (2011) can also be neglected because no S was detected in the Cr-rich areas of the sample.

EMP analyses of both POIs considered indicate that the Cr-bearing phases are a mixture of $Cr(OH)_{3(am)}$ and Ca-Cr-hydrocalcite, whereas Fe is present as a Fe-S-containing phase, probably pyrite (see Table 3 for a list of minerals in the sample).

The two POIs studied reveal differences in the appearance of the Cr- and Fe-bearing solid phases (Figs. 4 and 5) and, in combination with the Eh-pH diagram (Fig. 6), point to two different evolution scenarios. For POI 1, where pyrite and $Cr(OH)_{3(am)}$ [+Ca-Cr-hydrocalcite] are not intimately associated (Fig. 4), we assume more acidic initial conditions, which allowed for precipitation of pyrite (Fig. 6). The conditions then changed to less acidic and more oxidizing, as documented by the measured prevailing Eh-pH conditions. This neutralization leads to precipitation of $Cr(OH)_{3(am)}$ [+Ca-Cr-hydrocalcite] in another part of the pore space (Fig. 4).

At POI 2, $Cr(OH)_{3(am)}$ [+Ca-Cr-hydrocalcite] and pyrite occur together in one grain (Fig. 5), which indicates that these phases precipitated under conditions that are represented by the overlapping stability fields of the two phases (Fig. 6) at moderately low pH. After

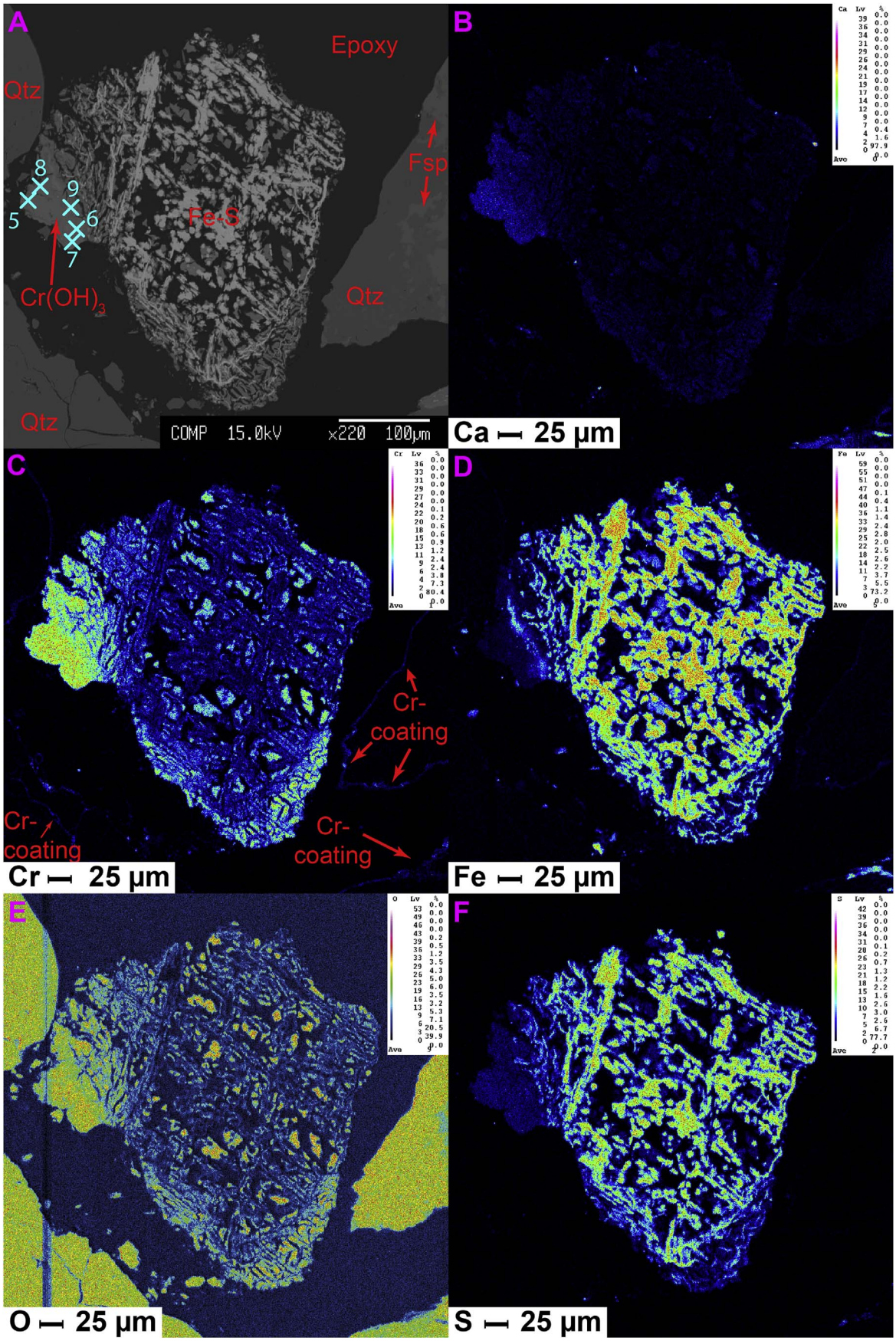

Fig. 5. Sample material from the black layer in the contaminated drill core C3 (POI 2): (A) BSE image. Marks indicate where the WDS analyses given in Table 2 were made. Distribution maps of Ca (B), Cr (C), Fe (D), O (E), and S (F) showing Cr-coated quartz (Qtz) and alkali feldspar (Fsp) grains. In the center, the BSE image and the element distribution maps display a grain of Fe-S and Cr phases.

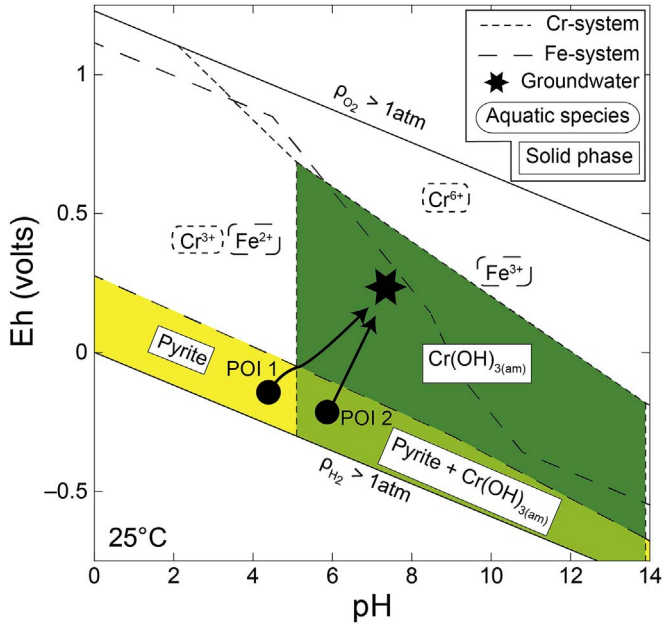

Fig. 6. Simplified combined Eh-pH diagram for the groundwater system showing predominant species of Cr and Fe (for individual systems, see Fig. S3). Input activities were: Al 3.66×10^{-05}, HCO_3 4.11×10^{-03}, Ca 1.92×10^{-03}, Cl 5.01×10^{-04}, Cr 3.80×10^{-05}, F 6.24×10^{-06}, Fe 3.54×10^{-05}, Si 1.03×10^{-06}, K 1.01×10^{-04}, Mg 5.69×10^{-04}, Mn 1.80×10^{-05}, N 3.66×10^{-04}, Na 6.87×10^{-04}, S 3.91×10^{-04}. The star indicates prevailing measured groundwater conditions (mean value). The full dots represent the possible initial conditions inferred from the textural associations in the two studied areas of sample C3 (POI 1 and POI 2). The arrows show possible paths from initial conditions to the Eh-pH conditions that can be measured today.

precipitation, conditions changed to less acidic and more oxidizing just as described above.

Additionally, POI 2 (Fig. 5) shows the Cr coating around grains of quartz and feldspar. This coating, which also contains some Ca but neither Fe nor S (see Fig. 5B, D and F), is also interpreted as consisting

Table 3
Summary of identified and inferred solid phases in the studied black layer material from drill core C3.

Mineral Name	Chemical Formula	Remarks
Quartz	SiO_2	identified by XRD
Albite	$NaAlSi_3O_8$	identified by XRD
Muscovite	$KAl_2(Si_3Al)O_{10}(OH)_2$	identified by XRD
Chlorite	$(Mg,Fe)_5(Al,Si)_5O_{10}(OH)_8$	identified by XRD
Pyrite	FeS_2	inferred from EMP data
Ca-Cr-hydrocalcite	$CaCr_2^{3+}(CO_3)_2(OH)_4{\cdot}H_2O$	inferred from EMP data
Cr hydroxide	$Cr(OH)_3$	inferred from EMP data

of the described mixture of precipitated $Cr(OH)_{3(am)}$ and Ca-Cr-hydrocalcite. As such coatings were found throughout the entire sample, they probably explain the macroscopically visible green color of the dried core material (Fig. S1B).

The solubility of Cr-bearing phases was decreased due to the acid neutralization, documented by the near-neutral to slightly alkaline pH (7.1–7.9) of the groundwater, leading to the precipitation of Cr-bearing phases (Palmer and Puls, 1996; Rai et al., 1987; Sass and Rai, 1987). The Cr mobility is also controlled by the redox state. Infiltrating Cr(VI) was reduced to Cr(III) through the reduction capacity of the soil and groundwater and through the reduction strength of the organic reducing agent (treacle) added during the tannery process.

In the alluvial material of U2, U3, U4 and U8, no color change was observed, but these macroscopic observations in combination with chemical analytical results lead us to the following interpretation for the formation of the black layer. Above the black layer, above and below the groundwater table, Cr is present mostly as common Cr(VI)-bearing phases, such as chromatite ($CaCrO_4$) or in its precursor form $CaCrO_4$ *$2H_2O$, the hydrated counterpart of chromatite. Below a certain depth and below the groundwater table, Cr(VI) is reduced to Cr(III), leading to the precipitation of Cr(III) hydroxide along with the Ca-Cr-hydrocalcite. Such a scenario is consistent with near-surface groundwater being generally more oxidizing than waters at greater depths.

We conclude that no Cr(VI) is present within and below the black

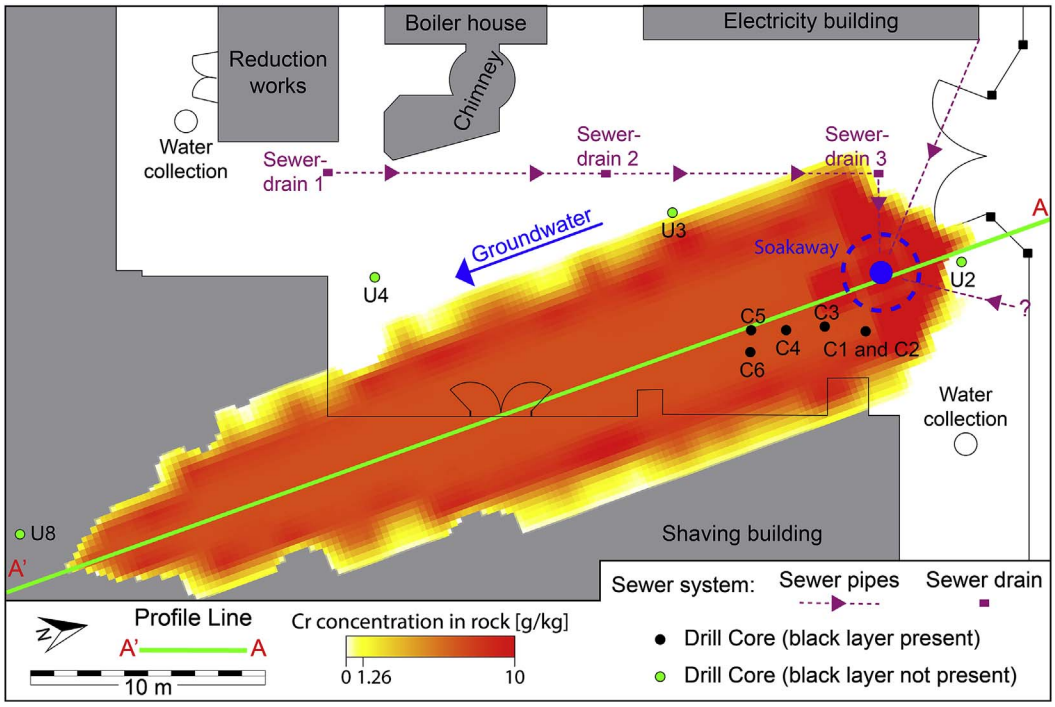

Fig. 7. Map of the northern area of the contaminated site (modified from Müller et al. (2007)) including the results of the 2-D model of the black layer: black dots = drill cores with black layer, green dots = drill cores with no black layer. (For interpretation of the references to colour in this figure legend, the reader is referred to the web version of this article.)

layer, even though drill core C6 (13.2–14 m) was the only sample where Cr(VI) was measured beneath the black layer. Due to the release of the organic reducing agent into the soakaway, infiltrating Cr(VI) is reduced and subsequently removed from the water through reduction-induced precipitation of $Cr(OH)_3$ and Ca-Cr-hydrocalcite. These precipitates form the black layer.

The sharp upper boundary of the layer can be explained as due to the natural reduction strength of groundwater, which increases with increasing depth, and to the presence of the organic reducing agent being required for the formation of the black layer. If the horizontal and vertical diffusion of this organic reducing agent is not fast enough, no black layer is formed, even though elevated $Cr_{(tot)}$ concentrations were detected in certain areas such as U3.

Based on the mineralogical investigations, precipitation was chosen to be the controlling factor for the mobility of Cr at this particular site, although the transport and, therefore, the residence time of Cr in the reservoir is influenced by many other processes (e.g., sorption). Precipitation of Cr-bearing phases is controlled by the reducing strength of the groundwater and the organic reducing agent, both causing the reduction of the Cr(VI) species that was introduced. Even though EMP analyses inferred the presence of the Ca-Cr-hydrocalcite ($CaCr_2^{3+}(CO_3)_2(OH)_4{\cdot}H_2O$) and $Cr(OH)_{3(am)}$, the Ca-Cr-hydrocalcite phase had to be neglected during the calculations of the Eh-pH diagram (Fig. 6) and the 2-D model (Fig. 7) due to a lack of thermodynamic data. Therefore, the dimensions of the black layer were modeled through precipitation of $Cr(OH)_{3(am)}$. The consumption of OH^- ions during precipitation of $Cr(OH)_{3(am)}$ causes a decrease in pH, which was prevented by adding a pH buffer ($Fe(OH)_{2(am)}$) to the model, yielding a neutral to slightly alkaline pH, which is consistent with the measured pH in the groundwater. Mineralogical and chemical investigations from the drill cores as well as the macroscopic color observations were used as input. Even though many parameters for the model had to be assumed, the boundary measurements ($Cr_{(tot)}$ concentrations of U3, U4 and U8) fit well with the calculation, which provides an estimate of the lateral extent of the contaminated black layer at the observed depth.

5. Conclusions

Using macroscopic observations as well as mineralogical and chemical characterization, the origin and genesis of the Cr contamination at an abandoned leather tannery were investigated. The results were used as input information for a 2-D model, which was developed to estimate the dimensions of a black Cr-containing layer at the site.

Our chemical and macroscopic observations reveal that the old soakaway must have been the source of the contamination, as suggested by four lines of evidence: 1) the black layer pinches out in the vicinity of the soakaway; 2) high $Cr_{(tot)}$ concentrations in the alluvial sediments around and downgradient of the soakaway; 3) high Cr(VI) leachability from the area obliquely below and around the soakaway; and 4) the confirmed existence and spreading of the black layer to the immediate south of the soakaway, parallel to the groundwater flow and no presence of the black layer in sediments from areas farther upgradient of the soakaway. Additionally, a black Cr-rich sludge, which appears to be a residue from the tannery acid production process, was discovered in the sewers that drain into this soakaway.

Chromium-containing residues from the tannery process are transported through the vadose zone into the groundwater where Cr(VI) is subsequently reduced and precipitated as $Cr(OH)_3$ and Ca-Cr-hydrocalcite, and forms the black layer along the direction of groundwater flow. Even though unequivocal identification of the precipitated Cr(III)-phase was not possible, we obtained information about the distribution of the contaminant in the aquifer.

The black layer represents the current extent of the Cr(III)-contamination, and the model estimates a lateral dimension of ~37 m (longitudinal) and ~10 m (transversal). This study demonstrates that the plume-shaped contamination will increase in size farther downgradient if the source of the Cr(VI)-containing material in the vicinity of the soakaway, above the black layer, is not removed. Even though the contamination contains mostly Cr(III), which is generally known to be bound in relatively insoluble mineral phases, mineralogical investigations indicated a rather unstable crystalline structure that makes these phases vulnerable to chemical reactions such as dissolution, which will lead to migration of the contamination farther downgradient.

Acknowledgments

The authors thank the Austrian Federal Ministry of Agriculture, Forestry, Environment and Water Management for funding the project “ChromSan” via the Kommunalkredit Public Consulting (B220010) in the program “Contaminated Site Remediation Research” and the Federal State of Carinthia for Co-Funding. We also want to thank the Austrian Federal Ministry of Agriculture, Forestry, Environment and Water Management for providing detailed analytical data, which were obtained during previous projects to investigate the potential risk to the environment of the contaminated site. Special thanks is extended to the Marshall Plan Foundation (651 844 19 15 2015), which funded a scholarship at the University of Pennsylvania for Philipp Sedlazeck, where some of the research for this paper was conducted. We are grateful to Federica Zaccarini for her help with the EMP analysis and to two anonymous reviewers and J. Holloway, Associate Editor, for the invaluable suggestions and comments.

Appendix A. Supplementary data

Supplementary data related to this article can be found at http://dx.doi.org/10.1016/j.apgeochem.2017.10.011.

References

Allmann, R., 2003. Röntgenpulverdiffraktometrie: Rechnergestützte Auswertung, Phasenanalyse und Strukturbestimmung ; mit 39 Tabellen, 2., korr. u. erw. Aufl. ed. Springer, Berlin u.a., 275 S.

Anderson, R.A., 1997. Chromium as an essential nutrient for humans. Regul. Toxicol. Pharmacol. 26 (1), S35–S41.

Avudainayagam, S., Megharaj, M., Owens, G., Kookana, R.S., Chittleborough, D., Naidu, R., 2003. Chemistry of chromium in soils with emphasis on tannery waste sites. In: Ware, G.W., Albert, L.A., Crosby, D.G., Voogt, P., de, Hutzinger, O., Knaak, J.B., Mayer, F.L., Morgan, D.P., Park, D.L., Tjeerdema, R.S., Yang, R.S.H., Gunther, F.A. (Eds.), Reviews of Environmental Contamination and Toxicology. vol. 178. Springer New York, New York, NY, pp. 53–91.

Barceloux, D.G., Barceloux, D., 1999. Chromium. J. Toxicol. Clin. Toxicol. 37 (2), 173–194.

Bijeljic, B., Blunt, M.J., 2007. Pore-scale modeling of transverse dispersion in porous media. Water Resour. Res. 43 (12).

Bradl, H.B., 2004. Adsorption of heavy metal ions on soils and soils constituents. J. colloid interface Sci. 277 (1), 1–18.

Calder, L.M., 1988. Chromium contamination of groundwater. Adv. Environ. Sci. Technol. 20, 215–229.

Chauhan, D., Sankararamakrishnan, N., 2011. Modeling and evaluation on removal of hexavalent chromium from aqueous systems using fixed bed column. J. Hazard. Mater. 185 (1), 55–62.

Costa, M., Klein, C.B., 2008. Toxicity and carcinogenicity of chromium compounds in humans. Crit. Rev. Toxicol. 36 (2), 155–163.

Cotton, F.A., Wilkinson, G., 1980. Advanced Inorganic Chemistry, 4 ed. ed. Wiley, New York, N.Y., pp. 1396.

DIN 38404-6. German Standard Methods for the Examination of Water, Waste Water and Sludge; Physical and Physico-chemical Parameters (Group C); Determination of the Oxidation Reduction (Redox) Potential (C 6). Deutsches Institut für Normungen, Berlin.

DIN 38405-24, 2003. German Standard Methods for the Examination of Water, Waste Water and Sludge; Anions (Group D); Photometric Determination of Chromium(VI) Using 1,5-diphenylcarbonohydrazide (D 24). ASI, Vienna.

DIN 38414-4, 1984. German Standard Methods for the Examination of Water, Waste Water and Sludge; Sludge and Sediments (Group S); Determination of Leachability by Water (S 4). Deutsches Institut für Normungen, Berlin.

DIN EN 25813, 1992. Water Quality; Determination of Dissolved Oxygen; Iodometric Method (ISO 5813:1983). german version EN 25813. Deutsches Institut für Normungen, Berlin.

DIN EN 27888, 1993. Water Quality; Determination of Electrical Conductivity (ISO 7888:1985). German version EN 27888.

DIN EN ISO 9963–1, 1995. Water Quality - Determination of Alkalinity - Part 1: Determination of Total and Composite Alkalinity (ISO 9963-1:1994). German version EN ISO 9963-1. ASI, Vienna.
Dresel, P.E., Qafoku, N., McKinley, J.P., Ainsworth, C., Liu, C., Ilton, E.S., Fruchter, J.S., Phillips, J.L., 2008. Geochemical Characterization of Chromate Contamination in the Vadose Zone of the 100 Areas at the Hanford Site PNNL-17674.
Földi, C., Dohrmann, R., Matern, K., Mansfeldt, T., 2013. Characterization of chromium-containing wastes and soils affected by the production of chromium tanning agents. J. Soils Sediments 13 (7), 1170–1179.
Gao, X., Schulze, D.G., 2010. Chemical and mineralogical characterization of arsenic, lead, chromium, and cadmium in a metal-contaminated Histosol. Geoderma 156 (3–4), 278–286.
Geelhoed, J.S., Meeussen, J., Lumsdon, D.G., Hillier, S., Roe, M.J., Thomas, R.P., Bewley, R., Farmer, J.G., Paterson, E., 2001. Modelling of chromium behaviour and transport at sites contaminated with chromite ore processing residue: implications for remediation methods. Environ. Geochem. Health 23 (3), 261–265.
GESTIS, 2006. Database on hazardous substances: information system on hazardous substances of the German Social Accident Insurance. http://gestis-en.itrust.de/nxt/gateway.dll?f=templates$fn=default.htm$vid=gestiseng:sdbeng Accessed 2 January 2017.
Grguric, B.A., Pring, A., Bevan, A.W.R., Downes, P.J., 2006. The minerals of comet vale, western Australia. Aust. J. Mineralogy 12 (1), 9–23.
Höllen, D., Stöllner, Markus, Pleßl, Katharina, Niesenbacher, I., Treimer, R., Lehner, M., 2016. Schlacken und Aschen für CO2-Speicherung und Verwertung. Deutsche Gesellschaft für Abfallwirtschaft.
ISO 10523, 2012. Water Quality - Determination of PH (ISO 10523:2008). German version EN ISO 10523.
ISO 5667-3, 2012. 2012. Water Quality Sampling -Part 3: Preservation and Handling of Water Samples. ASI, Vienna.
Kagis, 2017. Kärnten atlas. http://gis.ktn.gv.at/atlas/init.aspx?karte=atlas_basiskarten Accessed 28 August 2017.
Latimer, W.M., 1952. The Oxidation States of the Elements and Their Potentials in Aqueous Solutions, 2 ed. ed. Prentice-Hall, Englewood Cliffs, N.J., pp. 392.
Loncnar, M., van der Sloot, H.A., Mladenovic, A., Zupancic, M., Kobal, L., Bukovec, P., 2016. Study of the leaching behaviour of ladle slags by means of leaching tests combined with geochemical modelling and mineralogical investigations. J. Hazard. Mater. 317, 147–157.
Loyaux-Lawniczak, S., Lecomte, P., Ehrhardt, J.-J., 2001. Behavior of hexavalent chromium in a polluted groundwater: redox processes and immobilization in soils. Environ. Sci. Technol. 35 (7), 1350–1357.
Müller, P., Lorber, K.E., Mischitz, R., Weiss, C., 2014. Implementation of fluidized granulated iron reactors in a chromate remediation process. Sci. total Environ. 485–486, 748–754.
Müller, P., Lorber, K.E., Staber, W., Herrera, D., Hohl, S., Kubicek, A., Novak, J., 2007. In-situ Sanierung von Chromschäden Durch Reduktionsprozesse: Zwischenbericht. Montanuniversität Leoben, Leoben.
Nemes, F., Neubauer, F., Cloetingh, S., Genser, J., 1997. The Klagenfurt Basin in the Eastern Alps: an intra-orogenic decoupled flexural basin? Tectonophysics 282 (1–4), 189–203.
ÖNORM EN 15443, 2015. Solid Recovered Fuels — Methods for the Preparation of the Laboratory Sample. ASI, Vienna.
ÖNORM EN ISO 10304-1, 2009. Water Quality - Determination of Dissolved Anions by Liquid Chromatography of Ions - Part 1: Determination of Bromide, Chloride, Fluoride, Nitrate, Nitrite, Phosphate and Sulfate (ISO 10304-1:2007). German version EN ISO 10304-1:2009. ASI, Vienna.
ÖNORM EN ISO 17294-2, 2016. Water Quality - Application of Inductively Coupled Plasma Mass Spectrometry (ICP-MS) - Part 2: Determination of Selected Elements Including Uranium Isotopes (ISO 17294-2:2016). German version EN ISO 17294-2:2016. Vienna, ASI.
ÖNORM S 2088-1, 2004. Contaminated Sites - Risk Assessment Concerning the Pollution of Groundwater Which Is to Be Safeguarded. ASI, Vienna.
ÖNORM S 2092. Contaminated Sites - Sampling of Groundwaters. ASI, Vienna.
Palmer, C.D., Puls, R.W., 1996. Natural Attenuation of Hexavalent Chromium in Groundwater and Soils. EPA Ground Water Issue EPA154015–941505. EPA.
Palmer, C.D., Wittbrodt, P.R., 1991. Processes affecting the remediation of chromium-contaminated sites. Environ. Health Perspect. 92, 25–40.
Pawlikowski, M., Szalińska, E., Wardas, M., Dominik, J., 2006. Chromium originating from tanneries in river sediments: a preliminary investigation from the upper dunajec river (Poland). Pol. J. Environ. Stud. 15 (6), 885–894.
Petrucci, R.H., Harwood, W.S., 1993. General Chemistry: Principles and Modern Applications, 6. ed. ed. Macmillan, New York, pp. 19.
Qafoku, N.P., Evan Dresel, P., Ilton, E., McKinley, J.P., Resch, C.T., 2010. Chromium transport in an acidic waste contaminated subsurface medium: the role of reduction. Chemosphere 81 (11), 1492–1500.
Rai, D., Sass, B.M., Moore, D.A., 1987. Chromium(III) hydrolysis constants and solubility of chromium(III) hydroxide. Inorg. Chem. 26 (3), 345–349.
Royal Society of Chemistry, 2015. ChemSpider: search and share chemistry. http://www.chemspider.com/Search.aspx?rid=e1cd404c-0447-4d4b-bc66-bbee21fb7444 Accessed 1 June 2016.
Rudnick, R.L., Gao, S., 2003. 3.01-Composition of the continental crust. In: Holland, H.D., Turekian, K.K. (Eds.), Treatise on Geochemistry. Elsevier, pp. 1–64.
Salminen, R., Batista, M., Bidovec, M., Demetriades, A., Vivo, B., de, Vo, de, s.W., Duris, M., Gilucis, A., Gregorauskiene, V., Halamic, J., Heitzmann, P., Lima, A., Jordan, G., Klaver, G., Klein, P., Lis, J., Locutura, J., Marsina, K., Mazreku, A., O'Connor, P., Olsson, S., Ottesen, R., Petersell, V., Plant, J., Reeder, S., Salpeteur, I., Sandström, H., Siewers, U., Steenfelt, A., Tarvainen, T., 2005. Geochemical Atlas of Europe: Part 1-Background Information, Methodology and Maps. IUGS/IAGC Global Geochemical Baselines, Finland.
Sass, B.M., Rai, D., 1987. Solubility of amorphous chromium(III)-iron(III) hydroxide solid solutions. Inorg. Chem. 26 (14), 2228–2232.
Sedlazeck, K.P., Höllen, D., Pomberger, R., 2015. Chromium contaminated site – but where is the chromium?, in: Österreichische Mineralogische Gesellschaft (ÖMG) (Ed.), Mitteilungen der Österreichischen Mineralogischen Gesellschaft.
Sokol, E.V., Gaskova, O.L., Kokh, S.N., Kozmenko, O.A., Seryotkin, Y.V., Vapnik, Y., Murashko, M.N., 2011. Chromatite and its Cr3+- and Cr6+-bearing precursor minerals from the nabi musa mottled zone complex, judean desert. Am. Mineralogist 96 (4), 659–674.
Umweltbundesamt, 2013. Altlast K22 “Lederfabrik Neuner” Gefährdungsabschätzung und Prioritätenklassifizierung (§13 und 14 Altlastensanierungsgesetz), Wien.
UTC, 2012. Endbericht Ergänzende Untersuchungen gemäß § 14 AlSAG – Altlast K 22 „Lederfabrik Dr. Hans Neuner“, Klagenfurt.
Wanner, C., Eggenberger, U., Kurz, D., Zink, S., Mäder, U., 2012a. A chromate-contaminated site in southern Switzerland – Part 1: site characterization and the use of Cr isotopes to delineate fate and transport. Appl. Geochem. 27 (3), 644–654.
Wanner, C., Eggenberger, U., Mäder, U., 2012b. A chromate-contaminated site in southern Switzerland – Part 2: reactive transport modeling to optimize remediation options. Appl. Geochem. 27 (3), 655–662.
Wiberg, K.B., 1965. Oxidation by Chromic Acid and Chromyl Compounds: Oxidation in Organic Chemistry. Part a. pp. 115 New York, London.
Yuan-Hui, L., Gregory, S., 1974. Diffusion of ions in sea water and in deep-sea sediments. Geochimica Cosmochimica Acta 38 (5), 703–714.
Zhu, M., Liu, Y., 1981. Discovery of native chromium in xizang (tibet). Chin. Sci. Bull. 26 (11), 1014–1017.